Numerical identification of mechanisms triggering 2D choke flutter in transonic fan

Quentin Rendu, Stéphane Aubert, Pascal Ferrand

To cite this version:

Quentin Rendu, Stéphane Aubert, Pascal Ferrand. Numerical identification of mechanisms triggering 2D choke flutter in transonic fan. Journal of Fluids and Structures, 2020, 97, pp.102879. 10.1016/j.jfluidstructs.2020.102879 . hal-03234686

Version of Record: https://www.sciencedirect.com/science/article/pii/S0889974619302257
Manuscript_d59761b8206a90785629e7754fdcced1

International Forum on Aeroelasticity and Structural Dynamics
IFASD 2017
25-28 June 2017 Como, Italy

IDENTIFICATION OF 2D CHOKE FLUTTER TRIGGERS IN TRANSONIC FAN

Q. Rendu[1], **S. Aubert**[1], **P. Ferrand**[1]

[1]Université de Lyon
ECL, LMFA UMR CNRS 5509
36 av. Guy de Collongue, 69134 Ecully, France
q.rendu@imperial.ac.uk

Abstract: Blade vibration may trigger a self-induced aeroelastic instability (flutter). In turbomachinery choke flutter appears when a strong shock-wave chokes the blade passage. The aim of this study is to identify mechanisms responsible for the instability. An innovative methodology relying on the splitting of the emitter and receiver role of the blade is presented. It is successfully applied to 2D linearised RANS computations of choke flutter. The emission splitting shows that the vibration of the blades downstream of the shock-wave generates a backward travelling pressure wave triggering the aeroelastic instability. The reception splitting demonstrates the destabilising contribution of the shock-wave / separated boundary layer interaction. The source of flutter is finally a combination of inviscid (regressive waves) and viscous (unsteady separation) mechanisms.

Keywords: aeroelasticity, flutter, turbomachinery, fan, linearized RANS, acoustic blockage

1 INTRODUCTION

Flutter is a critical self-induced aeroelastic instability which can lead to the failure of fan blades. In high bypass ratio transonic fan, this instability appears at part speed regimes, typically around 80% of the nominal rotational speed. The type of flutter encountered depends on the operating point along the speedline. Choke flutter is observed at low incidence (either slighlty positive or negative), which corresponds to high massflow and low pressure ratio. The steady flow is subsonic upstream of the blade row and supersonic in the blade passage. A strong shock-wave chokes the passage and interacts with the boundary layer on both the suction side and the pressure side. If strong enough, this shock-wave / boundary layer interaction (SWBLI) can lead to the separation of the flow. The blades vibration generate pressure and velocity fluctuations through different sources interacting with each other:

- the fluctuations of incidence result in pressure fluctuations on the blade surface
- the no-slip condition on a vibrating blade generates a velocity fluctuation
- the area variation of the blade passage triggers shock-wave oscillation
- the separation or oscillation of the boundary-layer may act as an acoustic source
- the vibrating trailing edge acts as an acoustic source

In 1975, Mikolajczak et al. [1] stated that incidence and shock-wave contributions are two viable candidates to explain choke flutter. Tanida et al. [2] performed experiments on the influence of solidity on choke flutter. They established that the solidity must be sufficiently high for choke flutter to be triggered. They also reported an influence of the shock-wave steady position and its interaction with the boundary-layer. Jutras et al. [3] confirmed the influence of solidity and introduced the destabilising contribution of the reduced velocity, the inlet pressure and the inlet temperature. The high contribution of the shock-wave oscillation to choke flutter is confirmed by an experimental study of Micklow et al [4]. Srinivasan [5] presented 20 parameters affecting the aeroelastic behavior of rotating blades for stall, choke and supersonic flutter. The list includes geometric parameters (solidity, blade twist), aerodynamic variables (tip speed, incidence, shock-wave position, distortion) and structural ones (frequency, mode shape, mistuning).

To obtain local information on the unsteady flow, computational methods have been developed. In turbomachinery computational aeroelasticity, the blade stability is generally obtained through the energetic method [6]. This method relies on the radial decomposition of the 3D blade in a sum of 2D airfoils. The damping coefficient is computed on each 2D airfoil and the overall damping coefficient is obtained by an integral along the radius, from hub to tip. The region close to the tip usually shows the highest contribution to the global damping coefficient, because velocity and pressure fluctuations are the largest. At part-speed, for stall flutter, the maximal contribution is found between 80% and 90% span [7,8]. Concerning the flow modelling, Petrie-Repar et al. [9] show that viscous effects are important at off-design conditions (near stall and choke).

Despite all these efforts, the physical mechanisms driving choke flutter are not yet understood [10]. The interaction of many influential parameters partly explains this complexity. A decomposition method relying on linear superposition principle can be used to decouple some of them. This approach has been used by Ferrand [11] to analyse choke flutter contributions using a coupled 1D/2D linearised Euler method.

This work extends the decomposition method to 2D linearised Reynolds-Averaged Navier-Stokes (RANS) computations. The final objective is the identification of physical mechanisms driving choke flutter in a transonic fan. Methods are presented in the first section. They include the case setup, such as the fan geometry, the operating point and the structural modeshape, as well as the numerical solvers used in this work. The results are then exposed, starting with the verification of the linearised solver and the identification of a choke flutter instability. The decomposition method is then successfully applied to extract the sources of the instability. Finally, the local analysis of the extracted work allow us to reveal two mechanisms driving choke flutter.

NOMENCLATURE

$\delta\mathbf{x}$	blade displacement vector
π_t	total pressure ratio
σ	interblade phase angle
ζ	damping coefficient
ω	pulse
c	sound celerity

g	interblade pitch
j	imaginary number
k	reduced frequency
tke	turbulent kinetic energy
$\dot{m}$	mass flow
M	mach number
ND	nodal diameter
Nn	rotational speed
Ps	static pressure
S	blade surface normal vector
T	vibration period
t	time
U	flow velocity
$\mathcal{U}$	vibrational kinetic energy
V	blade velocity vector
$\mathcal{W}$	work extracted by the flow
x	axial coordinate
x	coordinates vector
y	blade to blade coordinate
y^+	normalised wall distance
$\tilde{z}$	complex number $\tilde{z}$
$\lvert\tilde{z}\rvert$	modulus of complex number $\tilde{z}$
$\Phi\left(\tilde{z}\right)$	argument (phase) of complex number z
$\mathrm{Re}(z)$	real part of complex number z
$\mathrm{Im}(z)$	imaginary part of complex number z
${}^1\tilde{z}$	complex amplitude of first harmonic of z
$\widetilde{z_1}^* \cdot \widetilde{z_2}$	Hermitian inner product of $\widetilde{z_1}$ and $\widetilde{z_2}$

2 METHODS

2.1 Numerical solvers

The compressible RANS solver Turb'Flow is used in this work to compute the 2D steady flow and the reference unsteady flow. This solver relies on vertex centred finite volume method on multi-block structured grids [12]. Convective fluxes are obtained through upwind scheme of Roe [13] with Monotonic Upstream-centred Scheme for Conservative Laws (MUSCL) interpolation of third order [14]. The interpolation order is reduced in strong gradient zones according to Harmonic Cubic Upwind Interpolation (H-CUI) limiter. Diffusive fluxes are obtained through central interpolation of conservative variables. For steady computations, the pseudo time discretisation relies on backward Euler with CFL=20 and local time step to speed up the convergence. The linear problem arising from the implicit method is solved through GMRES iterative method [15]. For time-accurate unsteady computations, the time discretisation relies on a dual time-stepping method [16]. The flow is considered fully turbulent and the k-ω turbulence model of Wilcox [17] has been used.

The Linearised RANS (LRANS) solver Turb'Lin is used to compute the harmonic flow around the steady state. This solver has been previously validated on transonic separated flows [18,19]. The solution is obtained in the frequency domain by solving the linear system. Spatial discretisation relies on JST centred scheme [20] with linearised pressure sensor. Previous work have shown that the frozen turbulence assumption is not valid for separated flows [18,19]. The solver has been validated against transonic aeroelastic experimental data in [21].

2.2 Transonic fan

The aeroelatic behaviour of the transonic UHBR fan ECL5v1 is studied in this work. This geometry is the first design of ECL5, a 1/4 scaled model representative of UHBR future fans and dedicated to the experimental investigation of aeroelastic and aerodynamic instabilities. This work is part of a project which aims at designing a transonic fan exhibiting choke flutter. The operating range of ECL5v1 is plotted in Figure 1 for three different rotational speeds (nominal speed Nn=10450rpm). The maximum isentropic efficiency, not shown here, varies between 90% and 95% depending on the rotational speed.

A 2D blade passage mesh has been extracted at 90% of ECL5v1 span to run the aeroelastic study. The sketch of the blade surface, presented in Figure 2, shows thin, highly staggered blades with low camber, which is typical of transonic fan tip airfoils. The operating point chosen for the aeroelastic studies corresponds to the lowest pressure ratio on the 0.8Nn speedline (see Figure 1).

The mesh used for both steady and unsteady computations has been obtain through a convergence study. It consists in 106,007 points with $y^+ < 1$ for the first cell layer at the blade surface. Total pressure, total temperature and azimuthal velocity are imposed at the domain inlet and static pressure is imposed at the domain outlet.

The steady relative Mach number associated with the choked flow is plotted in Figure 3. Looking at the leading edge zone, negative incidence can be seen as well as a supersonic region choking the blade passage and terminated by a strong shock-wave. On the pressure side, the

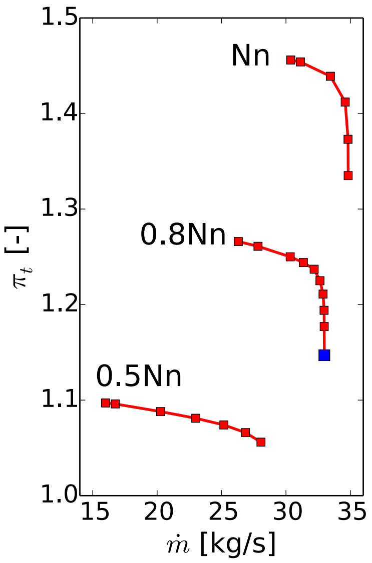

Figure 1: Operating range of ECL5v1 - choked operating point in blue

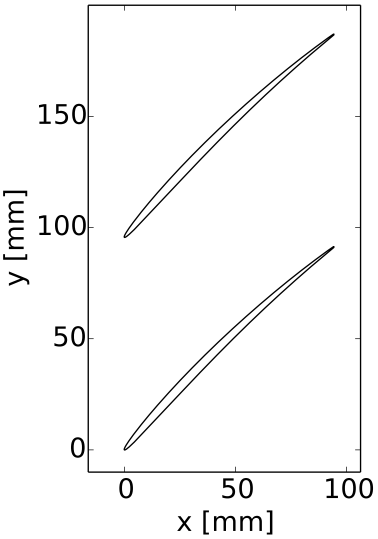

Figure 2: Sketch of aerodynamic airfoils at 90% span

maximal Mach number is 1.23 and the boundary layer is attached to the blade downstream of the shock-wave. On the suction side, the Mach number reaches 1.32 which leads to the separation of the boundary layer downstream of the shock-wave. The separation is closed and the reattachment point is located 8.3% of chord downstream of the separation point.

2.3 Structural setup

Transonic flutter generally occurs along the first 3D bending mode of the blade. Projected on a 2D plane, this yields a rigid body motion, *i.e.* without deformation of the blade surface. In this study, the modeshape consists in a rotation of the airfoil around its leading edge. This modeshape has been chosen as it exhibits choke flutter with significant negative aerodynamic damping. Three different positions of the blade during a vibration cycle are plotted in Figure 4.

In turbomachinery aeroelaticity, the motion of adjacent blades is coupled. For tuned blades, the frequency and modeshape are identical but a phase shift exists between two adjacent blades, called interblade phase angle or IBPA. Because of the annular periodicity of the rotor, the IBPA can only reach discrete values. In the reference frame of the rotor, it can be seen as a circumferential travelling wave. The IBPA is by convention positive when the wave propagates in the same direction than the rotor speed and negative otherwise.

Flutter usually appears for positive IBPA lower than 90°. In this work, the two extremes IBPA 0°and 90°are investigated. A sketch of the blades position during the vibration cycle for these two phase shifts is plotted in Figure 5. It can be seen for $\sigma = 90^\circ$ that the adjacent blades motion are out of phase. This leads to a maximal area fluctuation which in turn leads to strong velocity fluctuations.

To model the blade vibration in frequency domain, the complex amplitude of displacement $\widetilde{\delta \mathbf{x}}$ and velocity $\widetilde{\mathbf{V}}$ are imposed at each node of the blade mesh. The steady position of the blade is chosen as the phase origin. This yields

$$\mathrm{Re}(\widetilde{\delta \mathbf{x}}) = 0 \quad ; \quad \mathrm{Im}(\widetilde{\mathbf{V}}) = 0 \tag{1}$$

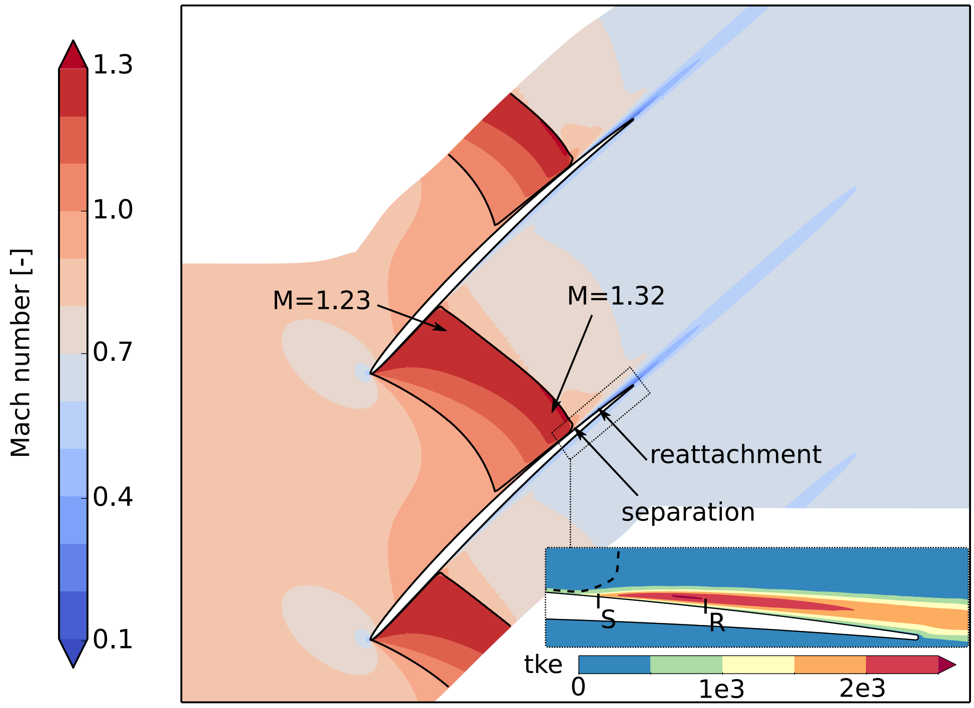

Figure 3: Steady relative Mach number for choked flow and field of turbulent kinetic energy (tke) in the separated region

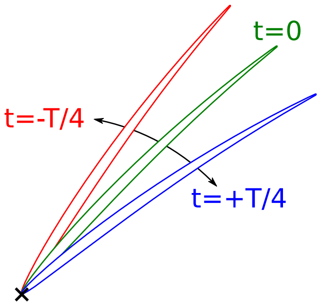

Figure 4: Sketch of three blade positions during a vibration cycle - rotation around leading edge

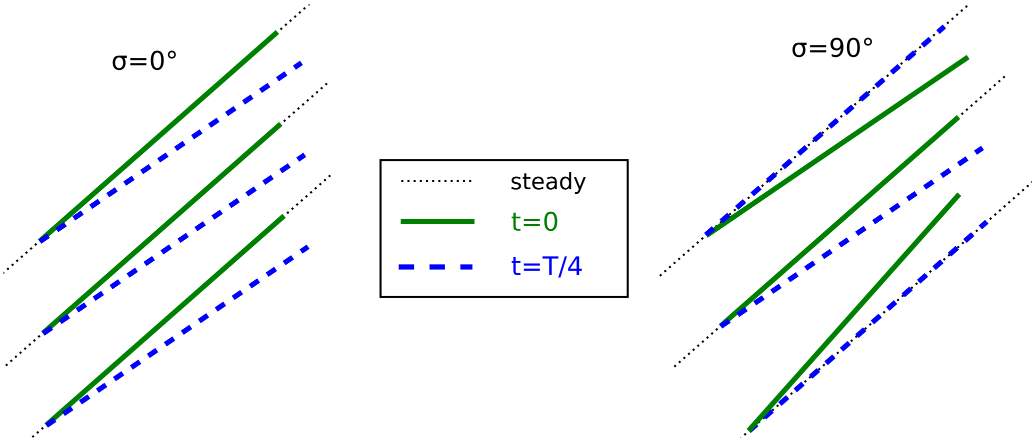

Figure 5: Sketch of blades position during a vibration cycle for $\sigma = 0^\circ$ and $\sigma = 90^\circ$ (steady blade position in black dashed lines)

The interblade phase angle (IBPA) σ is modelled through quasi-periodic boundary conditions in azimuthal direction

$$\widetilde{q}(x_b + g) = \widetilde{q}(x_b)e^{j\sigma} \tag{2}$$

where $\widetilde{q}$ is the complex amplitude of conservative variable fluctuations, x_b the domain boundary and g the interblade pitch.

The work $\mathcal{W}$ extracted by the flow to the structure is written according to the convention of Verdon [22]. The damping coefficient is then obtained by the integral of the extracted work along the blade surface

$$\zeta = \frac{1}{4\pi} \frac{\iint_\Omega \mathcal{W} \mathrm{d}\Omega}{\mathcal{U}} \tag{3}$$

where Ω is the fluid-structure contact interface and $\mathcal{U}$ the maximal vibrating kinetic energy. The work can be written as

$$\mathcal{W} = \int_0^T \left[-\widetilde{Ps}(\mathbf{x}, t) * \mathbf{S}(\mathbf{x}, t) \right]^* \cdot \widetilde{\mathbf{V}}(\mathbf{x}, t) \mathrm{d}t \tag{4}$$

where $\widetilde{Ps}$ is the instantaneous static pressure, $\mathbf{S}$ the vector associated with the instantaneous surface, oriented towards the structure, and $\widetilde{\mathbf{V}}$ the instantaneous velocity vector associated with the blade displacement. In frequency domain, neglecting second order terms, the only contribution to the unsteady work is, for a rigid body motion,

$$\mathrm{Re}(\,^1\widetilde{Ps})\,\mathbf{S} \cdot \mathrm{Re}(\,^1\widetilde{\mathbf{V}}) \tag{5}$$

where $^1\widetilde{Ps}$ and $^1\widetilde{\mathbf{V}}$ are the complex amplitude of first harmonic of static pressure and velocity vector, respectively. Thus only the real part of fluctuating static pressure contributes to the stability of the fluid-structure interaction.

2.4 Decomposition method

According to superposition principle, the unsteady flow generated by the vibration of the whole blade is equal to the sum of unsteady flows generated by the vibration of each surface mesh node. The blade motion can thus be decomposed in an arbitrary number of zones N and the global damping coefficient can be computed by the sum of the damping coefficient associated with each motion. Formally,

$$\zeta = \sum_i^N \zeta_i \quad ; \quad \zeta_i = \frac{1}{4\pi\mathcal{U}} \iint_\Omega \mathrm{Re}(\,^1\widetilde{Ps_i})\,\mathbf{S} \cdot \mathrm{Re}(\,^1\widetilde{\mathbf{V}}) \mathrm{d}\Omega \tag{6}$$

where $\widetilde{Ps_i}$ represents the pressure fluctuations generated by the motion of zone i. Regarding flutter, the blade can be seen both as an emitter and a receiver of pressure fluctuations. The decomposition method splits the blade in several independent emitters. The definition of each zone should rely on physical insights.

3 RESULTS AND DISCUSSION

3.1 Influence of interblade phase angle (IBPA)

In this section the reduced frequency based on the blade chord is $k = 0.15$ (quasi-steady flow). Linear and nonlinear methods are compared at IBPA $\sigma = 0^\circ$ in Figure 6. The amplitude,

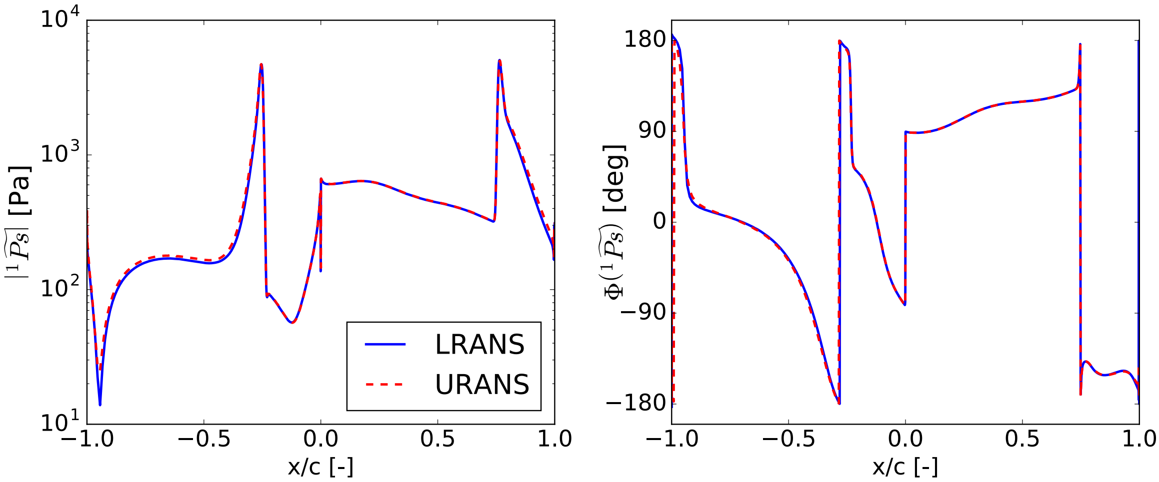

Figure 6: Amplitude (left) and phase (right) of pressure fluctuations on blade surface from linearised (TBL) and nonlinear (TBF) computations at $k = 0.15$ and $\sigma = 0^\circ$ (x/c = 0 denotes the leading edge, negative abscissa denotes the pressure surface, positive abscissa the suction surface)

plotted on the left, show two large peaks corresponding to the impact of the shock-wave on the pressure and suction side. Close to perfect agreement is observed both on amplitude and phase, demonstrating the ability of the linearised method to predict the unsteady loads on the blades

The linearised method is now used to investigate the influence of IBPA on aeroelastic stability. The real part of pressure fluctuations for $\sigma = 0^\circ$ is plotted on the left in Figure 7. The largest fluctuations can be seen around the steady position of the shock-wave (dashed black line) as well as in shock-wave / boundary layer interaction regions. The pressure fluctuations associated with the shock-wave motion at the center of interblade passage and close to the wall are out of phase. This may indicate a high contribution of viscous effects in shock-wave / boundary layer interaction regions. It can also be observed that pressure fluctuations almost vanish upstream and downstream of the shock-wave.

The real part of pressure fluctuations for $\sigma = 90^\circ$ is plotted on the right in Figure 7. The fluctuations levels are larger than those observed for $\sigma = 0^\circ$ in every part of the flow. This is a direct consequence of the large velocity fluctuations induced by the area variations for $\sigma = 90^\circ$. Locally, the stronger fluctuations occur near the steady shock-wave position and in shock-wave / boundary layer interaction regions. For this IBPA, large fluctuations are also observed upstream of the blades and in the interblade passage downstream of the shock-wave.

To analyse the aeroelastic stability, the extracted work is plotted along blade chord in Figure 8 for both IBPA ($\sigma = 0^\circ$ and $\sigma = 90^\circ$). Leading edge is at $x/c = 0$, negative abscissa corresponds to the pressure side and positive abscissa to the suction side. Upstream of the steady shock-wave ($-0.25 < x/c < 0.75$), the extracted work is very low for both IBPA which corresponds to a neutral contribution to stability (neither stabilising nor destabilising). On the pressure side, the shock-wave shows a destabilising contribution ($x/c = -0.25$) for both IBPA. This contribution is larger for $\sigma = 90^\circ$ because of larger pressure fluctuations (see Figure 7). Downstream of the steady shock-wave ($-1.0 < x/c < -0.25$), a neutral contribution is observed for $\sigma = 0^\circ$ while it is stabilising for $\sigma = 90^\circ$.

On the suction side, the contribution of the shock-wave motion is opposite for the two IBPA. For $\sigma = 0^\circ$, the contribution is stabilising and 2.5 times larger than the pressure side shock-

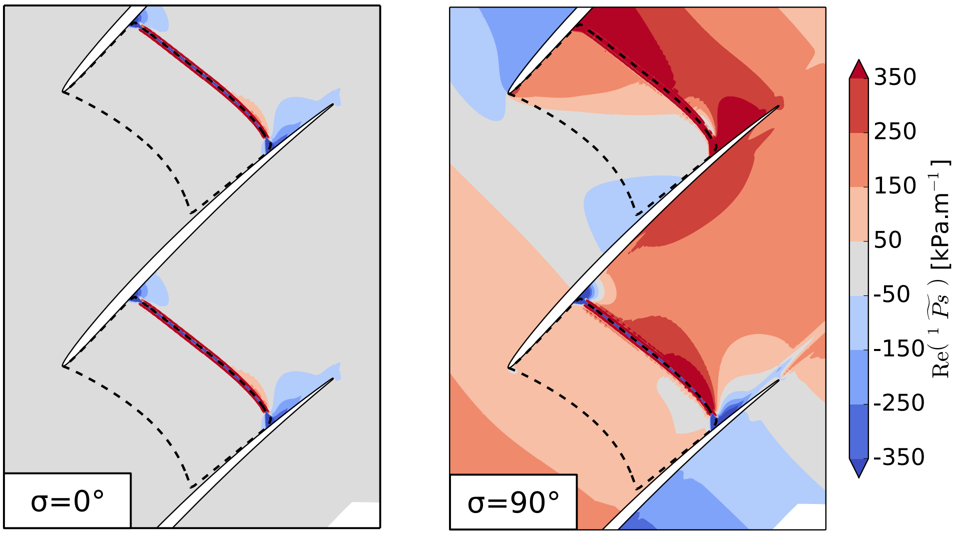

Figure 7: Real part of pressure fluctuations for $\sigma = 0^\circ$ (left) and $\sigma = 90^\circ$ (right) - $k = 0.15$

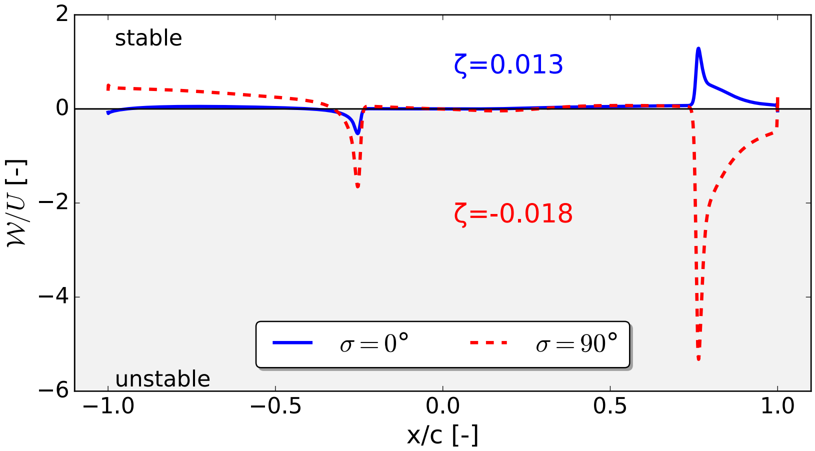

Figure 8: Extracted work along blade chord for $\sigma = 0^\circ$ and $\sigma = 90^\circ$ (leading edge at $x/c = 0$, pressure side: $x/c < 0$, suction side: $x/c > 0$) - $k = 0.15$

wave contribution. For $\sigma = \mathbf{90}^\circ$, the contribution is destabilising and 3.3 times larger than the pressure side shock-wave contribution. In both case, the separated boundary layer ($x/c > 0.8$) shows an important contribution (same sign than the shock-wave contribution). Note that the motion of the blade is parallel to the trailing edge surface, hence the extracted work is zero at $x/c = 1.0$.

The damping coefficient is computed through the integral of the extracted work along the chord (see Equation (3)). For $\sigma = 0^\circ$, the damping coefficient is positive ($\zeta = 0.013$) which corresponds to a stable configuration. However, for $\sigma = 90^\circ$, the damping coefficient is negative ($\zeta = -0.018$). This means that an aeroelatic instability (choke flutter) occurs at reduced frequency $k = 0.15$ for the IBPA $\sigma = 90^\circ$.

To further investigate the local unsteady flow associated with choke flutter, the amplitude of entropy fluctuation is plotted in Figure 9 for the choke flutter case ($\sigma = 0^\circ$). The shock-wave oscillation induces large entropy fluctuations, both in the middle of the passage and at the separation point (impact of the shock-wave on suction surface). Another important contribution is found downstream of the trailing edge. Large fluctuation is also observed above the trailing

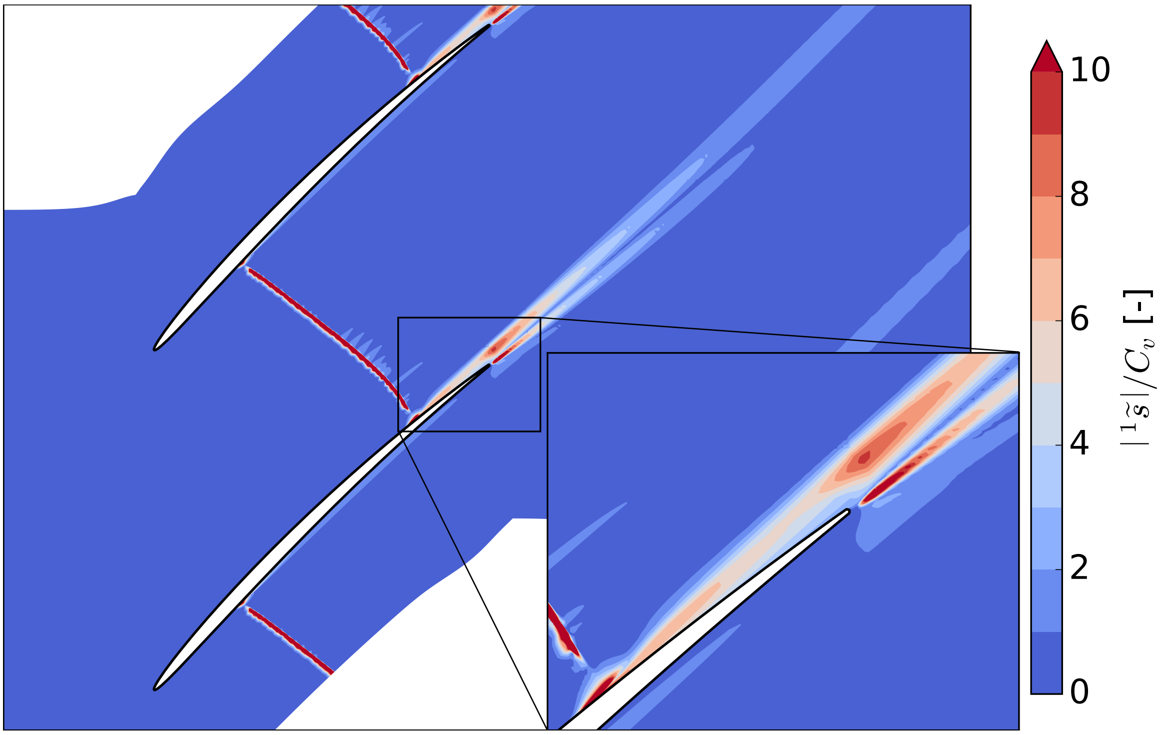

Figure 9: Amplitude of entropy fluctuation in blade passage

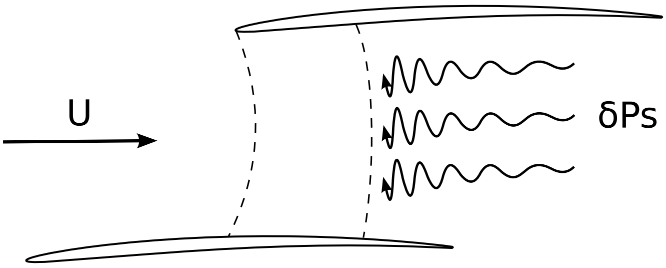

Figure 10: Acoustic blockage: wavelength decrease and amplitude increase of regressive pressure waves when approaching the shock-wave

edge. This probably results from the advected shear layer of the separated boundary-layer. Such a local analysis shows the competition of physical mechanisms: shock-wave oscillation, trailing edge vibration and separated boundary layer motion. In the next section, the decomposition method is used to decouple these mechanisms and obtain insights on the source of choke flutter.

3.2 Decomposition of excitation sources

In the previous section, a choke flutter event has been encountered at $k = 0.15$ and $\sigma = 90^\circ$. For choke flutter, previous studies have shown the important contribution of backward travelling pressure waves [23, 24]. Such waves are generated downstream of the shock-wave and propagate upstream with a velocity $c - U$ where U is the velocity of the steady flow and c the sound celerity. When reaching the shock-wave, the velocity of backward travelling pressure waves decreases which leads to an increasing of their amplitude. This phenomenon is a part of acoustic blockage, as described by Atassi et al. [25] and sketched in Figure 10.

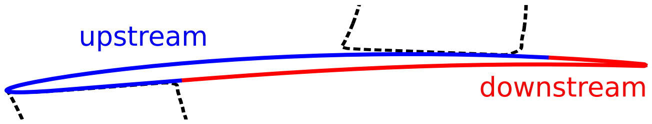

Figure 11: Blade surface decomposition in a downstream region (in red) and an upstream one (in blue)

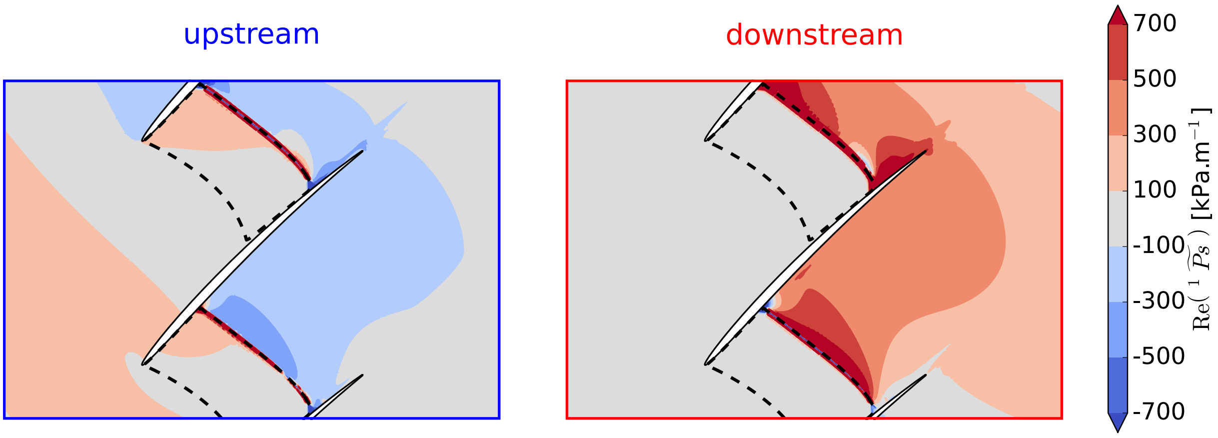

Figure 12: Real part of pressure fluctuations for upstream vibration (left) and downstream vibration (right) - $\sigma = 90^\circ$, $k = 0.15$

To identify the contribution of acoustic blockage to the overall aeroelastic response, the blade is cut into $N = 2$ different regions represented in Figure 11. The upstream region (in blue) extends form the leading edge to the shock-wave / boundary layer interaction region. On the suction side, where separation occurs, the upstream region extends until the reattachment point. On the pressure side, the flow is attached and the minimal friction coefficient has been chosen as the limit of the shock-wave / boundary layer interaction region. The downstream region (in red) corresponds to the remaining part of the blade. The vibration of the downstream part contributes to the unsteady flow through the generation of regressive waves. On the other hand, the vibration of the upstream part contributes through pressure waves (mainly generated at leading edge) and the local excitation of the shock-wave and the separated boundary layer on the suction side. Both parts act as an independent emitter, *i.e.* an independent source of unsteadiness. It has been verified that the sum of these two contributions is equal to the aeroelastic response when the entire blade vibrates.

The real part of pressure fluctuations associated with the upstream and downstream vibration is plotted in Figure 12. Looking at the upstream contribution (left), fluctuations occur in the interblade passage as well as upstream and downstream of the blade row. The fluctuations are larger in the vicinity of the steady shock-wave than in any other part of the flow. Concerning the downstream contribution (right in Figure 12), the fluctuations produced downstream of the shock-wave cannot travel through the supersonic zone. Indeed, no fluctuations are observed upstream of the shock-wave. In the downstream part of the flow, the largest fluctuations are seen in the vicinity of the steady shock-wave as well as in the sock-wave / boundary layer interaction region which indicates a high contribution of viscous effects.

To analyse the contribution of upstream and downstream motion to the stability, the extracted work is plotted for each contribution in Figure 13. Once again, the shock-waves are responsible for the largest part of the overall stability. For the upstream vibration, the shock-wave has a stabilising effect on both sides of the blade, the largest contribution being achieved on the suction

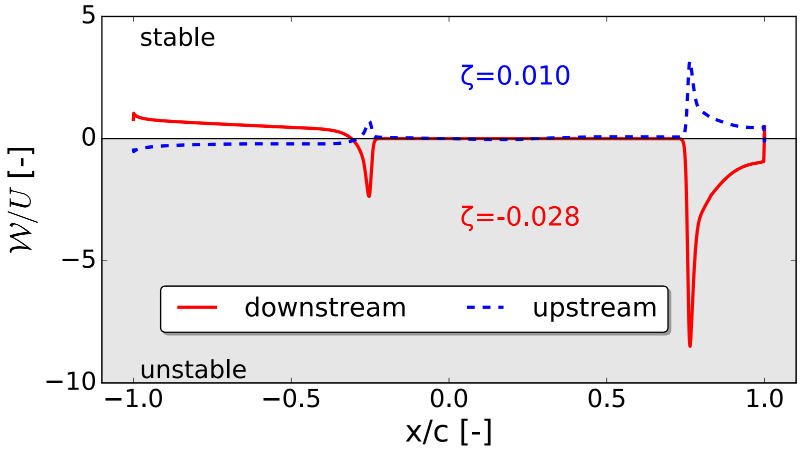

Figure 13: Extracted work along blade chord for upstream and downstream vibration - $\sigma = 90^\circ$, $k = 0.15$ (leading edge at $x/c = 0$, pressure side: $x/c < 0$, suction side: $x/c > 0$)

side where the boundary layer is separated. A noticeable destabilising contribution of the pressure side can also be seen downstream of the shock-wave. The aeroelastic response of the blade to the upstream vibration is stable ($\zeta = 0.010$). On the other hand, shock-wave has a destabilising effect for the downstream vibration on both sides. Once again, the destabilising contribution is larger on the suction side than on the pressure side. On the pressure side, a stabilising contribution is observed downstream of the shock-wave. The aeroelastic response of the blade to the downstream vibration is unstable ($\zeta = -0.028$). The upstream and downstream vibration contribute oppositely to the overall stability. Recall that the pressure fluctuations are higher for the downstream vibration because of acoustic blockage. Thus the aeroelastic behaviour of the blade is mainly driven by the downstream vibration at a reduced frequency $k = 0.15$.

The influence of reduced frequency on upstream and downstream vibration contribution to overall stability is now investigated for the IBPA $\sigma = 90^\circ$. The frequencies studied range from $k = 0.05$ to $k = 0.2$. For each frequency, two linear computations are run (one for the upstream vibration and one for the downstream vibration). The damping coefficient associated with each vibration is then computed. The product of damping coefficient by the pulse (normalised power) is plotted in Figure 14. This product represents the energy exchanged during a given time rather than during a vibration cycle.

The contribution of the downstream vibration is highly stabilising at low reduced frequency ($k = 0.05$). It then decreases, reaching a neutral contribution at $k = 0.10$ and a minimum at $k = 0.15$ where choke flutter has been encountered. The damping coefficient then rises and reach a neutral contribution at $k = 0.20$. The contribution of the upstream vibration behaves oppositely. It is indeed destabilising at low reduced frequency ($k = 0.05$) and increases until reaching a maximum at $k = 0.15$. It then decreases until reaching a neutral contribution at $k = 0.20$. Regarding the absolute value of the damping coefficient associated with each contribution, it can be seen that the downstream is always larger, except around $\mathbf{k} = \mathbf{0.10}$ where it reaches zero. This is a consequence of the amplification of regressive waves generated downstream of the shock-wave. As a result, the trend of the total damping coefficient is quite similar to the trend of the downstream contribution. This global analysis shows that the aeroelastic behaviour of the blade is driven by its downstream contribution independently of the reduced frequency.

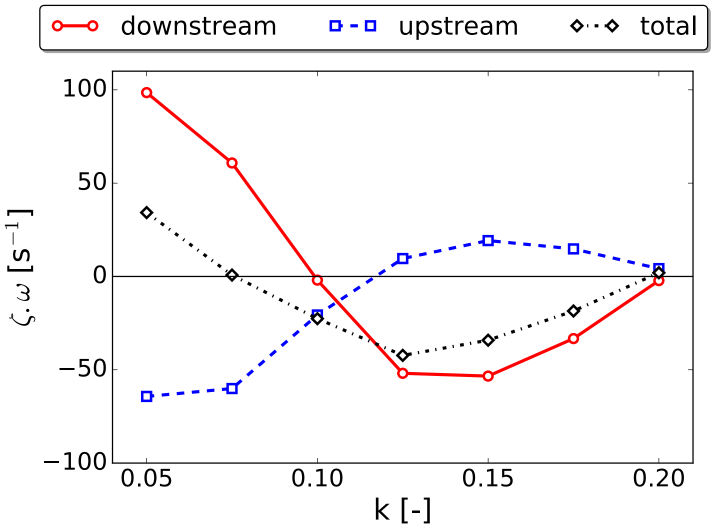

Figure 14: Normalised power associated with the upstream (in blue), downstream (in red) and total (black) vibration of the blade - $\sigma = 90\,^{\circ}$

3.3 Local analysis of destabilising work

The previous analysis showed that the downstream part of the blade emits pressure fluctuations driving the choke flutter instability. In this section, a local analysis is performed to identify the regions where energy is exchanged from the fluid to the structure.

The reception role of the blade is first splitted into two parts shown in Figure 15: the shock-wave / boundary layer interaction region (in red) and the aft region of the blade (in green). The SWBLI corresponds to the region from the shock-wave until the gradient of friction coefficient is equal to zero. The damping coefficient associated with each region is also plotted along reduced frequency. Independently of the reduced frequency, the aft region shows a positive damping coefficient. This indicates that in this region, the energy is extracted by the fluid to the structure (stabilising contribution). The variation of damping along reduced frequency is small, yet slightly decreasing. On the other hand, in the SWBLI region, the negative damping coefficient indicates that the fluid feeds energy into the structure (destabilising contribution). The variation of damping along reduced frequency is similar to the damping of the entire blade but shifted downwards. This shows that the choke flutter instability mainly results from the energy exchange in the SWBLI region.

The SWBLI region is now splitted again into two parts: pressure side and suction side. The damping associated with each region is plotted in Figure 16. The contribution of the pressure side is stabilising at low reduced frequency and slightly destabilising for high frequencies ($k \geq 0.20$). The suction side shows a strong destabilising contribution at all frequencies and exhibits a minimal damping at $k = 0.125$. The exchange of energy from the fluid to the structure is almost entirely localised in the suction side SWBLI region along a wide range of frequencies ($0.075 < k < 0.175$).

To analyse the local unsteady flow, the real part of pressure fluctuations is plotted in Figure 17. At low reduced frequency $k = 0.05$, the pressure fluctuations in the SWBLI region are weaker on the suction side than on the pressure side. For the suction side, even if the velocity is stronger, this leads to a smaller absolute value of damping coefficient (see Figure 16, $k = 0.05$). As the reduced frequency increases to $k = 0.10$, the pressure fluctuations increase in the SWBLI

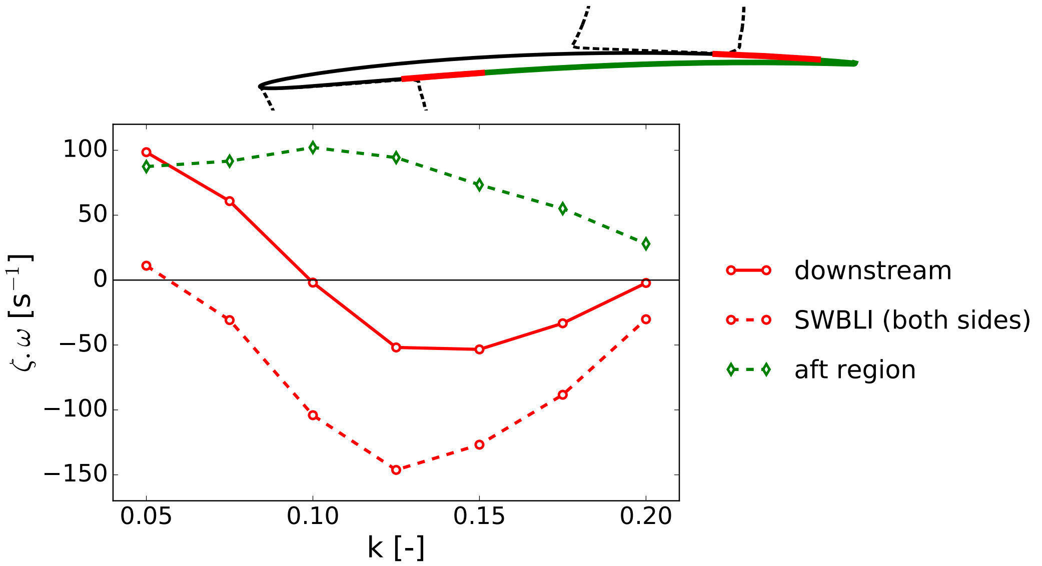

Figure 15: Damping of the SWBLI region, aft region and downstream region (sum of the previous two) along reduced frequency

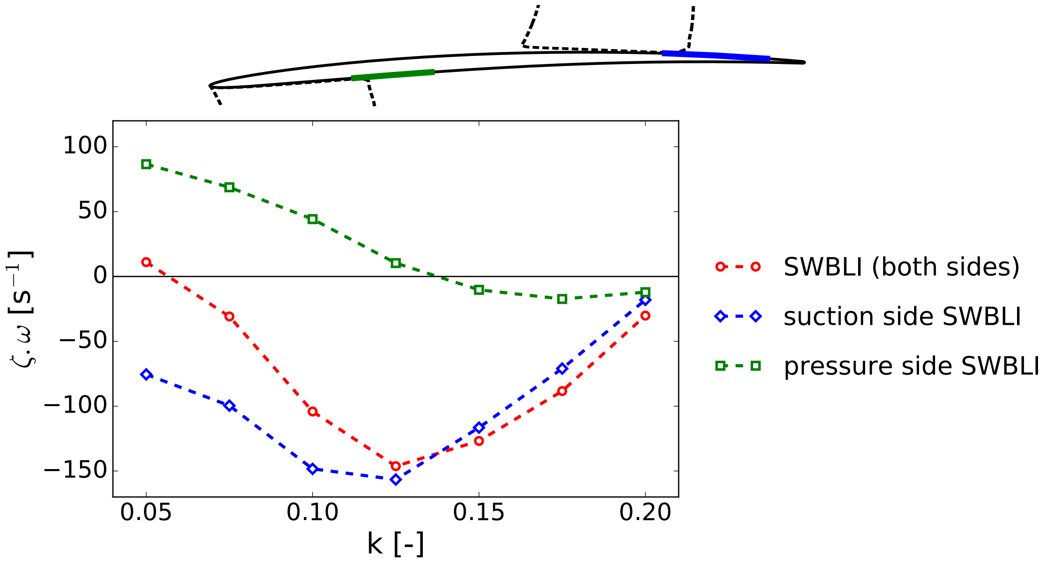

Figure 16: Damping associated with suction side SWBLI, pressure side SWBLI and SWBLI (sum of the previous two) along reduced frequency

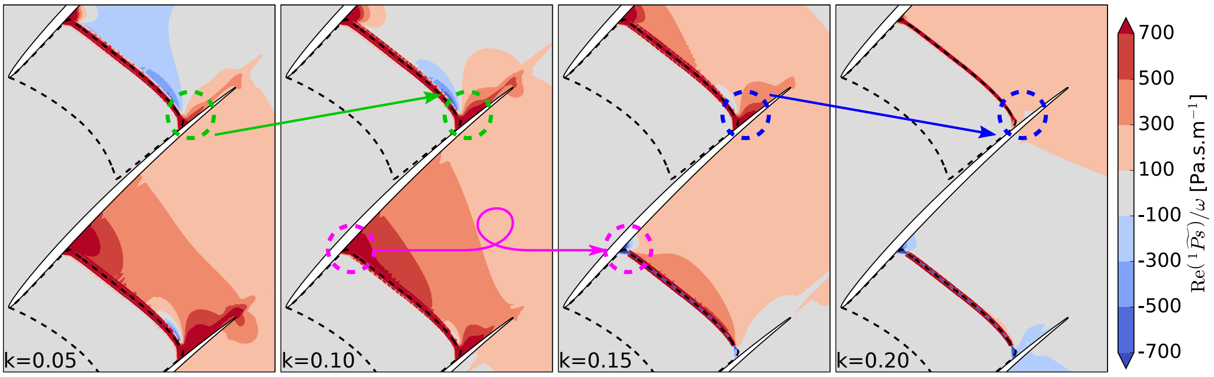

Figure 17: Real part of pressure fluctuations associated with the downstream vibration for different reduced frequencies at $\sigma = 90^\circ$ - in SWBLI regions : increase of pressure fluctuations in green, decrease in blue, inversion of the stability in magenta

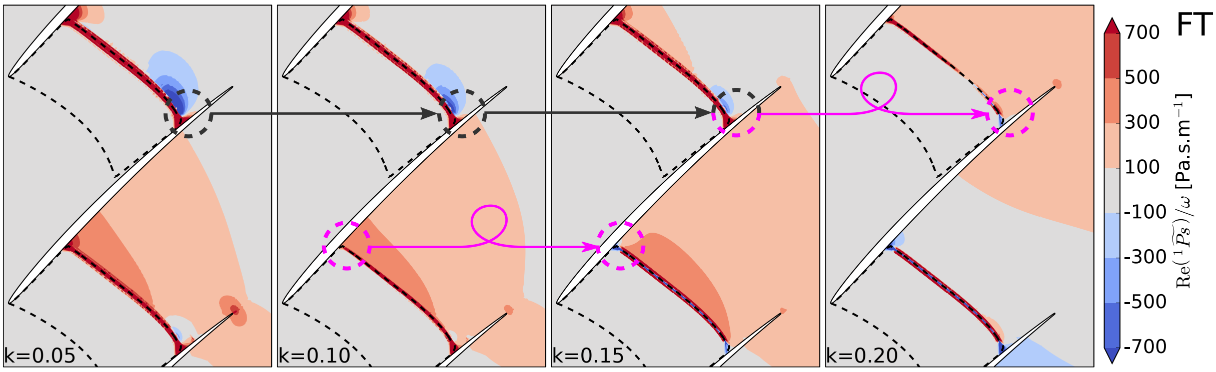

Figure 18: Real part of pressure fluctuations associated with the downstream vibration with constant turbulent viscosity (FT : frozen turbulence) for different reduced frequencies at $\sigma = 90^\circ$ - in SWBLI regions : stagnation of pressure fluctuations in grey, inversion of the stability in magenta

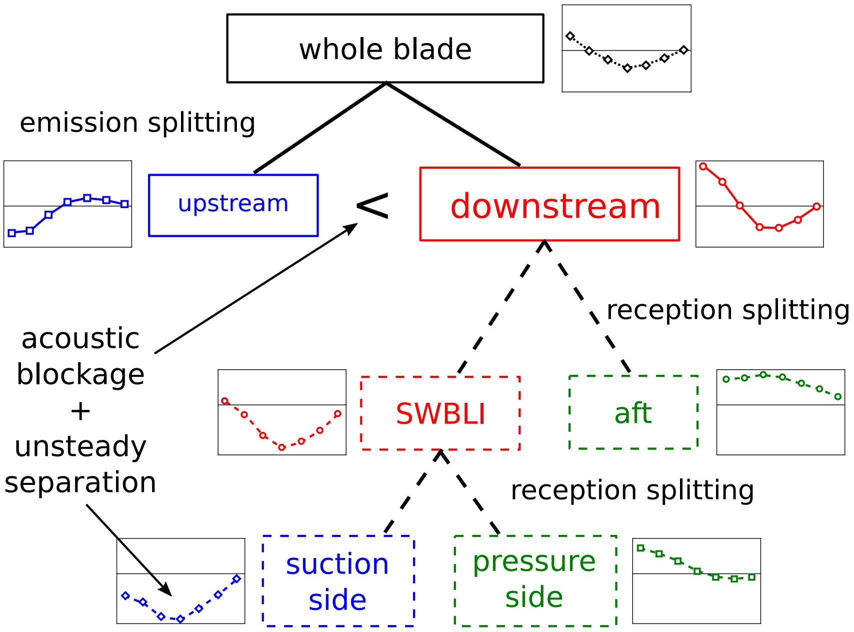

Figure 19: Summary of the methodology applied to identify the local sources of choke flutter instability (graphs represent damping coefficient along reduced frequency)

region on the suction side (green arrow), leading to a larger destabilising contribution. The magnitude of pressure fluctuations is now comparable between the pressure side and the suction side SWBLI region. From $k = 0.10$ to $k = 0.15$, the SWBLI contribution switches from stabilising to destabilising on the pressure side (magenta arrow). At the same time, the SWBLI zone becomes sharper on the pressure side while it is still wide on the suction side. From $k = 0.15$ to $k = 0.20$, the pressure fluctuations on the suction side decrease and almost vanish in the SWBLI region (blue arrow). The pressure side does not exhibit any change in the SWBLI region while the pressure fluctuations are lower behind it.

Differences have been observed between the unsteady behaviour of the SWBLI on the pressure and suction side. In the steady flow, the main difference between the pressure and suction side SWBLI is the separated boundary layer on the latter. The unsteady viscous effects associated with the separation could explain the differences aforementioned. To evaluate this hypothesis, frozen turbulence computations (*i.e.* constant turbulent viscosity with respect to time) have been run. The real part of the pressure fluctuations with constant turbulent viscosity is plotted in Figure 18. First, it can be observed that the SWBLI zones are very sharp with much lower magnitude of pressure fluctuations. This indicates a significant influence of unsteady viscous effects, particularly at low frequencies ($k \leq 0.10$) for which the differences are the largest. In the suction side SWBLI region, the pressure fluctuations do not vary from $k = 0.05$ to $k = 0.15$ (grey arrow) and then switches from a destabilising to a stabilising contribution between $k = 0.15$ and $k = 0.20$ (magenta arrow). On the pressure side, the SWBLI contribution is destabilising at high frequencies ($k \geq 0.15$) and very similar to the behaviour observed in Figure 17. The low frequencies ($k \leq 0.10$) are again associated with a stabilising contribution of the SWBLI. These results show that viscous effects influence the magnitude of the extracted work in weak SWBLI (on the pressure side) whereas it impacts both magnitude and sign in strong SWBLI (on the suction side).

4 CONCLUSION

This work aims at a better understanding of physical mechanisms responsible for choke flutter in transonic fan. The current design of the transonic research fan ECL5 has been used to support this study. A blade passage at 90% span has been chosen for the 2D aeroelastic analysis. The modeshape consists in a rigid body motion rotation around the leading edge with $\sigma = 0^\circ$ and $\sigma = 90^\circ$ interblade phase angles. State of the art nonlinear and linear RANS solvers were used to compute the steady flow and the linearised unsteady flow around the blades. A choke flutter event has been observed at reduced frequency $k = 0.15$ and for the interblade phase angle $\sigma = 90^\circ$.

A main contribution of this work is the extension of the decomposition method to 2D RANS computations the source of flutter instability. A summary of the methodology is plotted in Figure 19. The blade motion is decomposed into two independent parts (emission splitting). Results show that the aeroelastic behaviour of the blade is driven by regressive waves generated by the vibration of the downstream section of the profile.

Another contribution is the local analysis of the unsteady flow associated with the downstream vibration (reception splitting). Computing the damping coefficient for different zones, the largest contribution to stability has been associated with the unsteady shock-wave / separated boundary layer interaction on the suction side. The analysis of the pressure fluctuations in the interblade passage for different frequencies finally showed the major contribution of the unsteady viscous effects on the choke flutter instability.

The results on the importance of regressive waves open an interesting perspective for the design of choke flutter active control device. Piezoelectric actuators located near the rotor blade trailing edge or at the leading edge of the following stator blades can efficiently triggers or damps choke flutter in experimental facilities dedicated to aeroelastic studies.

The large contribution of unsteady viscous effects highlights the increasing need for local unsteady experimental data and may lead to new aeroelastic control concepts through the control of the separated boundary layer.

Finally, the linear decomposition method presented here is not limited to turbomachinery aeroelasticity and should be used whenever a deeper understanding of the unsteady flow is needed. The decomposition strategy should be adapted for each application. In case of nonlinear unsteady flow, one can evaluate the remaining coupling terms by withdrawing the linear response associated with each perturbation.

5 REFERENCES

[1] Mikolajczak, A., Arnoldi, R., Snyder, L., et al. (1975). Advances in fan and compressor blade flutter analysis and predictions. *Journal of Aircraft*, 12(4), 325–332.

[2] Tanida, Y. and Saito, Y. (1977). On choking flutter. *Journal of Fluid Mechanics*, 82(1), 179–191.

[3] Jutras, R., Stallone, M., and Bankhead, H. (1981). Experimental investigation of flutter in midstage compressor designs. *Journal of Aircraft*, 18(10), 874–880.

[4] Micklow, J. and Jeffers, J. (1981). Semi-actuator disk theory for compressor choke flutter. Tech. Rep. 19810016540, NASA.

[5] Srinivasan, A. (1997). Flutter and resonant vibration characteristics of engine blades. *Journal of Engineering for Gas Turbines and Power*, 119(4), 742–775.

[6] Marshall, J. and Imregun, M. (1996). A review of aeroelasticity methods with emphasis on turbomachinery applications. *Journal of Fluids and Structure*, 10.

[7] Aotsuka, M. and Murooka, T. (2014). Numerical analysis of fan transonic stall flutter. In *ASME Turbo Expo 2014: Turbine Technical Conference and Exposition*. Dsseldorf, Germany, June 16-20: American Society of Mechanical Engineers, p. V07BT35A020.

[8] Vahdati, M. and Cumpsty, N. (2016). Aeroelastic instability in transonic fans. *journal of Engineering for Gas Turbines and Power*, 138(2), 022604.

[9] Petrie-Repar, P. J., McGhee, A., Jacobs, P. A., et al. (2006). Analytical maps of aerodynamic damping as a function of operating condition for a compressor profile. In *ASME Turbo Expo 2006: Power for Land, Sea, and Air*. American Society of Mechanical Engineers, pp. 1133–1144.

[10] Dowell, E., Clark, R., Cox, D., et al. (2004). *A modern course in aeroelasticity*, vol. 3. Springer.

[11] Ferrand, P. (1984). Linearized theory of the choked flow in an annular oscillating cascade. In *Unsteady Aerodynamics and Aeroelasticity of Turbomachines and Propellers, 3rd International Symposium*. Cambridge, England, September: Ed Cambridge University, pp. 41–52.

[12] Smati, L., Aubert, S., Ferrand, P., et al. (1997). Comparison of numerical schemes to investigate blade flutter. *8th International Symposium of Unsteady Aerodynamics, Aeroacoustics and Aeroelasticity of Turbomachines*.

[13] Roe, P. (1981). Approximate riemann solvers, parameter vectors, and difference schemes. *Journal of computational physics*, 43(2), 357–372.

[14] Van Leer, B. (1979). Towards the ultimate conservative difference scheme. v. a second-order sequel to godunov's method. *Journal of computational Physics*, 32(1), 101–136.

[15] Saad, Y. and Schultz, M. (1986). GMRES : a generalized minimal residual algorithm for solving nonsymmetric linear systems. *SIAM Journal on Scientific and Statistical Computing*, 7(3).

[16] Jameson, A. (1991). Time dependent calculations using multigrid, with applications to unsteady flows past airfoils and wings. In *10th AIAA Computational Fluid Dynamics Conference*. Honolulu, HI.

[17] Wilcox, D. C. (1988). Reassessment of the scale determining equation for advanced turbulence models. *AIAA Journal*, 26(11).

[18] Philit, M., Ferrand, P., Labit, S., et al. (2012). Derivated turbulence model to predict harmonic loads in transonic separated flows over a bump. In *28th International Congress of Aeronautical Sciences*.

[19] Rendu, Q., Philit, M., Labit, S., et al. (2015). Time-linearized and harmonic balance Navier-Stokes computations of a transonic flow over an oscillating bump. In *14th International Symposium on Unsteady Aerodynamics, Aeroacoustics & Aeroelasticity of Turbomachines*. Stockholm, Sweden.

[20] Jameson, A., Schmidt, W., and Turkel, E. (1981). Numerical solution of the euler equations by finite volume methods using runge-kutta time-stepping schemes. In *14th AIAA Fluid and Plasma Dynamic Conference*. Palo Alto, CA.

[21] Rendu, Q., Rozenberg, Y., Aubert, S., et al. (2017). Influence of acoustic blockage on flutter instability in a transonic nozzle. *ASME J. Turbomachinery*, 140(2), 021004.

[22] Verdon, J. (1987). Linearized unsteady aerodynamic theory. In *AGARD Manual : Aeroelasticity in axial-flow turbomachines vol.1*. Platzer, M.F. & Carta, F.O.

[23] Ferrand, P. (1987). Parametric study of choke flutter with a linear theory. In *Advanced technology for aero gas turbine components*. AGARD CP 421.

[24] Rendu, Q., Rozenberg, Y., Aubert, S., et al. (2016). Investigation of shock-wave/boundary-layer interaction on aeroelastic stability : towards active control. In *ASME Paper GT2016-57302*. Seoul, South Korea.

[25] Atassi, H., Fang, J., and Ferrand, P. (1995). Acoustic blockage effects in unsteady transonic nozzle and cascade flows. In *33rd AIAA Aerospace Sciences Meeting*. Reno, NV, January 9-12, p. 303.